THE ASTROPHYSICAL JOURNAL, 505:984–992, 1998 October 1

GLOBAL SOLAR WIND CHANGES OVER SOLAR CYCLE 21: A COMBINATION OF *HELIOS* PHOTOMETER, IN SITU, AND INTERPLANETARY SCINTILLATION DATA

CH. LEINERT
Max-Planck-Institut für Astronomie, Königstuhl 17, D-69117 Heidelberg, Germany
AND
B. V. JACKSON
Center for Astrophysics and Space Sciences, University of California at San Diego 0424, La Jolla, CA 92093-0424
Received 1997 September 29; accepted 1998 May 4

ABSTRACT

We combine *Helios* spacecraft photometer brightnesses, in situ plasma densities, and interplanetary scintillation (IPS) velocity data to obtain a global description of solar wind changes. We find an increase of solar mass flux at solar maximum from the photometer brightnesses larger than would be expected from the usual assumption of invariant momentum flux over solar cycle 21 (1975-1986). A portion of this excess mass is related to solar mass ejections, which have an occurrence rate that follows the solar activity cycle.

Subject headings: interplanetary medium — solar wind — Sun: activity — sunspots

1. INTRODUCTION

Solar wind expulsion amounts to a significant fraction of the total solar mass loss, the major portion of which is from conversion of mass to energy in the Sun's interior. Since the reason for solar wind acceleration is still not known, it is necessary to map and understand this solar process globally. For stars with higher luminosities than the Sun, the process of stellar wind expulsion consumes an even larger percentage of stellar mass, and this can alter stellar evolution significantly (de Jager, Nieuwenhuijzen, & van der Hucht 1984). For the Sun, the one star we can study in detail, the global measurements over time discussed here lead to quantitative results that can serve as a reference for all stellar mass expulsion processes that populate interstellar space with particles.

We do not know how many different solar wind acceleration mechanisms there are. During times of solar activity minimum, solar wind flow is the most simple. At these times, more than 60% of the volume of the solar wind can be taken up by stable high-speed coronal hole winds, which expand nonradially near the solar surface to form the bulk of the heliosphere (Munro & Jackson 1977). At these times, the large-scale magnetic field divides the solar wind into two halves of opposite polarity roughly centered on the solar poles. At the maximum of the sunspot cycle, large coronal holes are absent and the picture is not so simple. At maximum, strong magnetic fields emanate from the solar surface up to approximately 35° away from the solar equator, and these regions influence the solar wind and contribute to it (Uchida et al. 1992; Hick et al. 1995). In addition, there are discrete expulsions of mass from the Sun, so-called coronal mass ejections (CMEs), that are related to these strong magnetic fields in that they are observed to have a strong correlation with the solar activity cycle (Webb & Jackson 1992; Webb & Howard 1994; see also Fig. 2 below). CMEs are obvious high concentrations of mass and energy in the solar wind. These ejections of mass can account for as much as 16% of the mass of the solar wind at the time of solar maximum (Jackson & Howard 1993), but only about 1% at solar minimum. The bulk of the solar wind flux has no such dramatic change with solar activity cycle, even though there is a marked change in the relative portions of high- and low-speed wind.

Direct observations of solar wind density and velocity are made in situ by spacecraft plasma probes. Solar wind observations by *Mariner 2* and *Helios 1* showed a relationship between proton density and plasma velocity, which Steinitz & Eyni (1980) interpreted as an invariance in momentum flux density carried by the protons in different types of solar wind flow. Mullan (1983) combined similar parameters using *ISEE-3* data near 1 AU, and came to the same conclusions for two different portions of the solar cycle. Bruno et al. (1986), using in situ *Helios* observations in the ecliptic plane, showed that plasma density and velocity during solar cycle 21 are approximately constant with distance from the heliospheric current sheet when combined as solar wind momentum flux.

The recent in situ record from the *Ulysses* spacecraft, which is probing polar solar winds at distances greater than ≈ 1.4 AU from the Sun, gives an account at high heliographic latitudes. The complete south polar passage of *Ulysses* summarized from early 1992 to 1995 for different solar wind parameters (Phillips et al. 1995) shows that momentum flux remains nearly constant with latitude, at least to the same extent as, if not more so than, the other parameter combinations studied. A more complete study of momentum flux measurements from *Ulysses* observations is given by Goldstein et al. (1996).

In some of the studies previously mentioned, the in situ data have been edited so that contaminant regions of solar wind interaction are removed from the record (e.g., Steinitz & Eyni 1980). Another obvious contaminant in detailed short-term analyses in the solar wind are the regions containing CMEs. However, even without temporal editing, the equatorial in situ record (as in Mullan 1983) favors a constant momentum flux. This implies either that CMEs do not dominate the ecliptic results to any appreciable extent, or that they are part of the result. Taken together, these in situ data provide substantial evidence for the concept of momentum flux invariance.

Remote sensing techniques have also been applied to

studies of fundamental solar wind parameters. Some of the first of these analyses (Bertaux & Lallement 1984) used *Prognoz 5* and *6* spacecraft Lyα photometer measurements of neutral hydrogen backscatter to determine solar wind parameters (Lallement et al. 1984). Interstellar neutral hydrogen atoms that penetrate the solar system are gradually ionized, primarily by collisions with the outward-moving solar wind protons. Models of this solar wind flux indicate a polar value in the years 1976 and 1977 that is only about half the equatorial value (Lallement, Bertaux, & Kurt 1985). Assuming a polar solar wind velocity of 800 km s^{-1} (as measured nearly two decades later by *Ulysses*), we find that this implies that the momentum flux is approximately constant between the pole and the equator during these years. In a detailed comparison of *Helios* photometer brightness changes and interplanetary scintillation (IPS) velocities, Hick & Jackson (1994), using approximate methods, show for the years 1975–1977 that among mass, momentum, and energy flux, momentum flux is best conserved between fast and slow regions at different solar latitudes and longitudes. Thus, for limited periods of time and for neighboring structures, remote sensing techniques and in situ measurements both support momentum flux invariance.

To our knowledge, global solar wind velocity and density changes over the solar cycle have not been thoroughly explored prior to this. At low latitudes, in situ measurements show that momentum flux is constant over the solar activity cycle to a good approximation (Schwenn 1990), but there is little long-term change in either velocity or mass. At high latitudes, a substantial solar cycle change of plasma brightness is observed in the *Helios* photometer record (Leinert & Pitz 1989), with a maximum approximately at solar activity maximum. The solar wind velocity over the solar poles observed in IPS measurements (Coles et al. 1980), on the other hand, shows a marked solar cycle change, with a decrease at maximum corresponding to the smaller extent of the polar solar coronal hole area at that time. We hypothesize that under the assumption that solar wind momentum flux is constant with heliographic latitude and from minimum to maximum of the solar cycle, the anticorrelation between these two effects could be understood as a natural outcome. To check this hypothesis and to quantitatively study global solar wind changes during solar cycle 21, we combine the three data sets described above. The in situ plasma measurements from *Helios* provide yearly averages of plasma density and velocity near the ecliptic from 1975 to 1983. The IPS observations provide solar wind velocity as a function of heliographic latitude over the same time interval. The combination of these data sets under the assumption of constant momentum flux enables us to determine a global density model that changes with solar cycle. The zodiacal light photometers measure brightness changes due to the electron density content at high heliographic latitude from 1975 to 1985, which are then used to determine the validity of the model. Section 2 presents the three different types of observations. In § 3, we determine a set of global solar wind models and compare their predictions with the observed brightness change. The models are unable to account for all the brightness increase seen in the *Helios* photometer data at solar maximum. In § 4, we discuss this result in terms of mass flux and coronal mass ejections as a possible source for the excess emission, and we conclude in § 5.

2. OBSERVATIONS: SOLAR CYCLE CHANGES

The geometric configuration of the Earth and *Helios 2* with respect to the Sun, along with the remote sensing views each provides, is shown in Figure 1.

Among our three data sets, the photometer observations have one limitation: they only give brightness *differences* with time. There is no direct way to separate the much greater zodiacal light brightness from the contribution of Thomson-scattered sunlight from solar wind plasma electrons. The unchanging portion of the solar wind density must be modeled globally to determine the total mass present. There is no similar restriction on either the IPS velocity measurements or the in situ measurements.

2.1. *Helios In Situ Data*

The *Helios* spacecraft remained within 0°.01 of the ecliptic plane throughout the experiment lifetime. The *Helios* in situ data have been analyzed in many different ways to investigate solar cycle effects (Schwenn 1990). We show a portion of these data crucial to our analysis. Figure 2 presents *Helios* in situ velocities (V), proton densities (n_p), mass flux ($n_p V$), momentum flux ($n_p V^2$) and energy flux ($n_p V^3$) from 1975 through 1985. Data from both *Helios 1* and *Helios 2*, ranging in heliocentric distance from 0.3 to 1.0 AU, are averaged after first normalizing to 1 AU by projecting observations outward proportional to r^{-2}. In situ ecliptic solar wind proton velocities decrease from about 500 km s^{-1} in early 1975 to below 400 km s^{-1} in 1980. The largest velocities correspond to times when the largest and most persistent high-speed streams reach the equator at the descending phase of the solar cycle ahead of activity minimum (Bame et al. 1976). Minimum solar wind speeds occur roughly at solar activity maximum. The average yearly in situ ecliptic solar wind proton density is modulated by about 20%. The high density in 1977 is due to an almost continuous presence of "quiet" slow solar wind during this time, coinciding with a heliospheric magnetic field reversal (current sheet) that is aligned with the solar equator (Schwenn 1990). The yearly average proton density from the beginning of 1975 until the end of *Helios 1* observations in 1985 averages to 7.8 protons cm^{-3} at 1 AU. Figure 2 also shows the NOAA smoothed sunspot numbers (Solar Geophysical Data 1982, 1987) as a reference showing solar activity. These numbers were used to identify the interval 1975–1977 as the "minimum" period and the interval 1979–1981 as the "maximum" period for the purposes of our study. The detailed features of the ecliptic solar wind proton fluxes show clear solar-cycle–related effects from comprehensive studies and interpretations of in situ and solar observations (Schwenn 1990). However, for the modeling described below, we determine nearly identical average ecliptic values for a proton density of 7.7 cm^{-3} for solar minimum and 7.9 cm^{-3} for solar maximum for use over the respective time periods of our study.

In the bottom panel of Figure 2 we also show the CME number rate curve, as measured by a variety of different spacecraft instruments (including the *Helios* photometers) during the same time interval (from Webb & Howard 1994).

2.2. *Interplanetary Scintillation*

IPS has been used to remotely sense the solar wind plasma since the early 1960s (Hewish 1964). This technique measures fraction-of-a-second intensity fluctuations in the

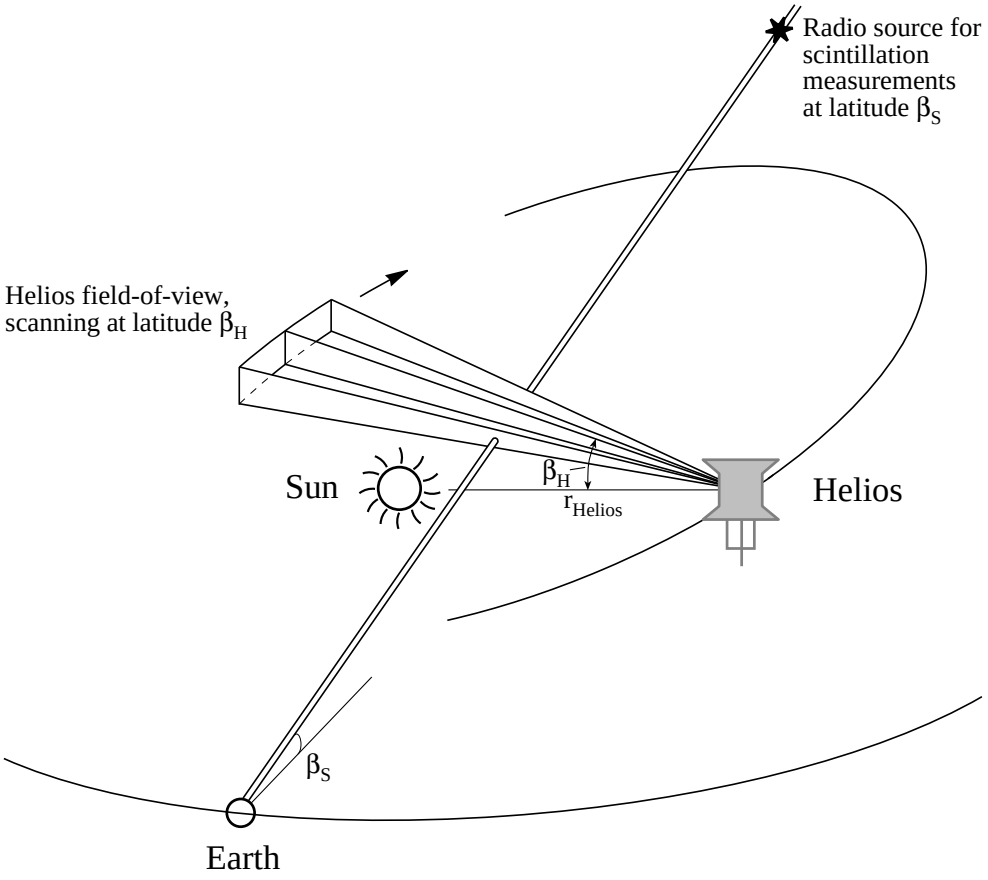

FIG. 1.—Example of the geometric configuration of the *Helios* and IPS measurements. A typical line of sight for a scintillation measurement is given (§ 2.2). The directions to the two 16° photometer sectors nearest the Sun are depicted at one position in the *Helios 2* spacecraft orbit (§ 2.3) to demonstrate the spatial overlap of the volumes scanned by the two techniques. β_H is the ecliptic latitude of the *Helios* photometer field of view, and it stays approximately constant during the rotation of the *Helios* spacecraft.

meter-wave radio signal strength from small-diameter radio sources. These fluctuations are caused by density inhomogeneities of a few hundred kilometers in size in the solar wind. IPS velocity measurements use multiple antennas located over baselines of a few hundred kilometers (Coles & Kaufman 1978). The solar wind speed can be deduced by cross-correlating time offsets in the intensity patterns. The University of California at San Diego (UCSD) IPS radio arrays operated at 73.8 MHz and obtained data daily from eight radio sources from 1972 to 1982. Useful solar wind speed estimates were typically obtained from 3–5 radio sources around the sky each day. IPS solar polar observations are not continuous, since they rely on the presence of radio sources crossing the solar poles. Northern polar observations were obtained from March to November each year, while southern polar observations were obtained from June to August. The IPS velocity data have long been used in a variety of ways to determine polar solar velocities. Coles et al. (1980) show from the UCSD data that polar solar wind speeds were higher at solar minimum than at solar maximum. More recently, the UCSD IPS data have been presented in the form of 6 month Carrington synoptic maps that show the general characteristics of the solar wind over the solar cycle (Rickett & Coles 1991). These earlier results have relied on an assumption that the IPS velocity measurement represents the solar wind at the closest approach of the line of sight to the Sun (point P approximation). In this way, the observed solar wind speed can be mapped to a specific heliographic latitude and longitude. One disadvantage of this method is that speed determinations at high latitudes will be biased toward lower values of velocity by the usually denser and slower equatorial solar wind in the foreground.

More recently, a different (tomographic) technique has been used to relate IPS observations to solar latitudes and longitudes (Jackson et al. 1998; Kojima et al. 1998). These least-squares fitting techniques rely on approximating the line-of-sight IPS response and, using perspective views from solar rotation and outward solar wind flow, mapping IPS velocities in heliographic latitude and longitude. These maps averaged over solar longitudes show velocities at high heliographic latitudes that average to 700–800 km s^{-1} at solar minimum (Kojima et al. 1998), consistent with *Ulysses* polar velocity measurements (Jackson et al. 1998). This technique also shows a sharp delineation at solar minimum between regions of high and low velocity. The tomographic technique is less restrictive in reconstructing velocities at high heliographic latitude than the point P approximation, since it relies on the presence of crossed perspective line-of-sight components to locate regions in latitude, and these crossings may occur beyond the point of closest approach. This feature makes it particularly useful for velocity determinations over the solar poles. The tomographic deconvolution comparisons of velocities sensed remotely with those measured in situ give satisfactory one-to-one results and show heliospheric structures at higher contrast than pre-

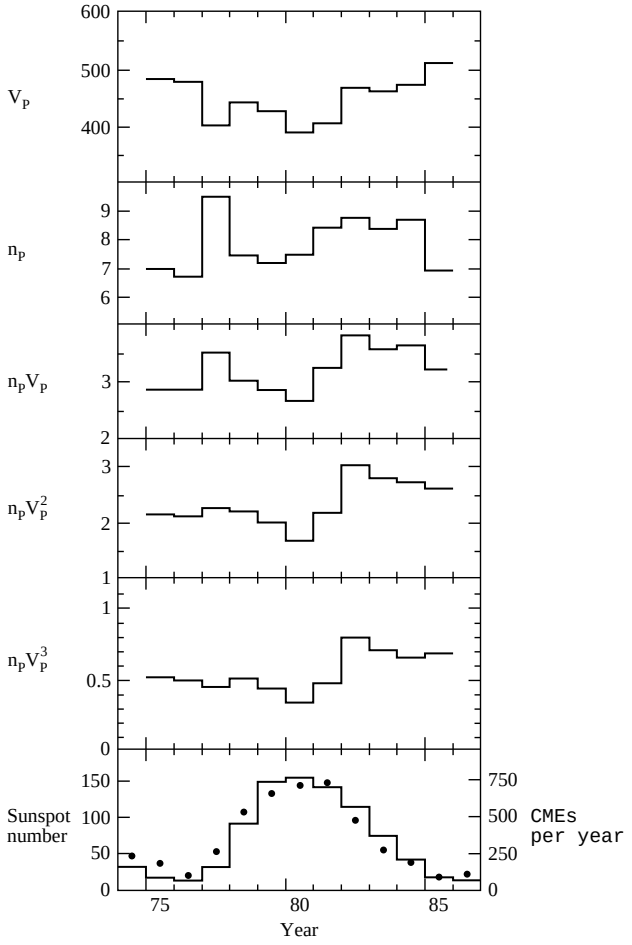

FIG. 2.—Yearly averages of solar wind quantities derived from the in situ measurements of the *Helios 1* and *Helios 2* space probes (Schwenn 1990). V_p, proton velocity in km s^{-1}; n_p, proton density in cm^{-3}; $n_p V_p$, proton flux density in 10^8 protons cm^{-2} s^{-1}; $n_p V_p^2$, momentum flux density in 10^8 dyne cm^{-2} s^{-1}; $n_p V_p^3$, kinetic energy flux density in erg cm^{-2} s^{-1}. The lowest panel shows the yearly averaged smoothed sunspot numbers (*histogram*) and the CME rate per year (*filled circles*).

viously possible (Jackson et al. 1998). This paper relies on the tomographically deduced velocities.

Figure 3 presents yearly averages of such velocity measurements obtained from the IPS data from 1975 through 1982. The data from all elongations $\geq 20°$ probed by the IPS analysis were used in the study. In all, the averages represent IPS velocity information from over 100 solar rotations (Carrington numbers 1609 through 1715). These velocity determinations clearly show the decrease in the average polar solar wind velocity from solar minimum to solar maximum, while the change in equatorial wind speeds is modest. Not unexpectedly, when we checked the analysis using the point P method, it failed to reproduce plasma velocity values that were as high over the poles at solar minimum.

2.3. *Helios Photometer Data*

The *Helios 1* spacecraft was launched in 1974 December; *Helios 2* followed in 1976 January. Both spacecraft are in elliptic orbits with perihelion at ≈ 0.30 AU and periods of close to half a year. The *Helios* zodiacal light sensors (Leinert et al. 1975; Leinert et al. 1981a) consist of three photometers rotating with the spacecraft on an axis perpendicular to the plane of the ecliptic. The photometers of *Helios 1* point 16°, 31°, and 90° south of the ecliptic plane, with the 16° and 31° photometers clocking data into 32 longitude sectors at constant ecliptic latitude around the sky. Sectors were numbered 1 through 32, beginning at the ecliptic longitude nearest the Sun in the direction of the spacecraft spin. The 16 sectors nearest the Sun have lengths of 5.°6 in ecliptic longitude; sectors at greater elongations have lengths of 11.°2 and 22.°4. The spacecraft photometer data were integrated over an 8.6 minute period in turn from each of the three photometers through a set of broadband ultraviolet, blue, and visual light filters and polarizers, and were refreshed in a data sequence lasting nominally 5.2 hr. *Helios 2* photometers point north of the ecliptic plane at positive ecliptic latitudes (Fig. 1), counterparts of those of *Helios 1*.

The 6 month cyclic brightness change observed by the *Helios* photometers due to the orbital motion has been presented in detail by Leinert et al. (1981b). When these orbital brightness changes are removed from the data and all remaining long-term changes are smoothed using a high-pass filter, significant short-term (≈ 1 day) brightness increases above background are observed. Richter, Leinert, & Planck (1982) first noted that the majority of these short-term increases correspond to plasma density enhancements

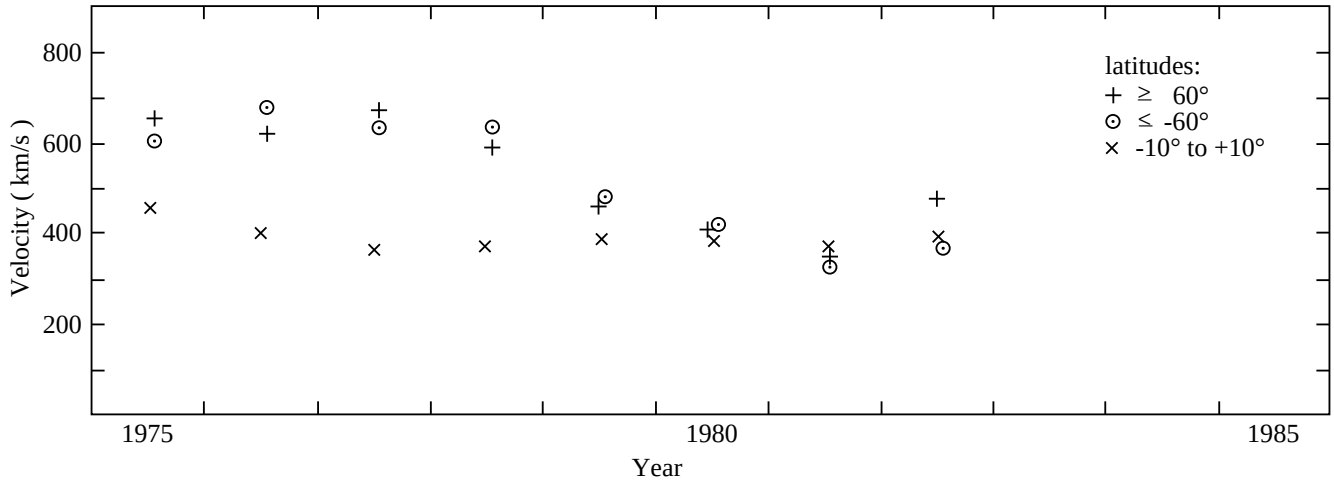

FIG. 3.—Solar wind velocities deduced from IPS measurements for solar cycle 21. Yearly averages are given for both polar regions and the equatorial zone. Note the decrease in polar wind speed from minimum to maximum.

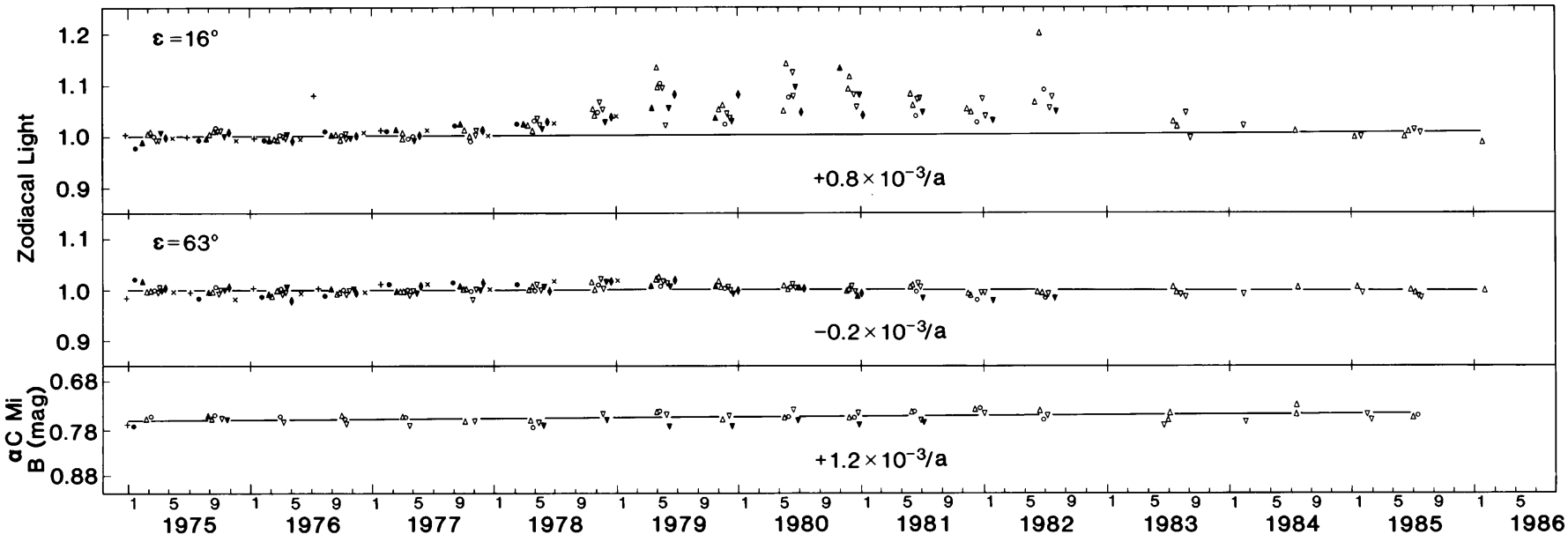

FIG. 4.—Relative changes of zodiacal light brightness observed with *Helios 1* at ecliptic latitude (see Fig. 1) of $\beta = -16°$ from 1974 December through 1986 February. Elongation value, $\epsilon = 16°$, refers to a viewing direction over the south pole of the Sun, $\epsilon = 63°$ to a viewing direction 62° east of the Sun. The bottom panel shows measurements of the bright star α CMi to the same scale to demonstrate the stability of the instrument.

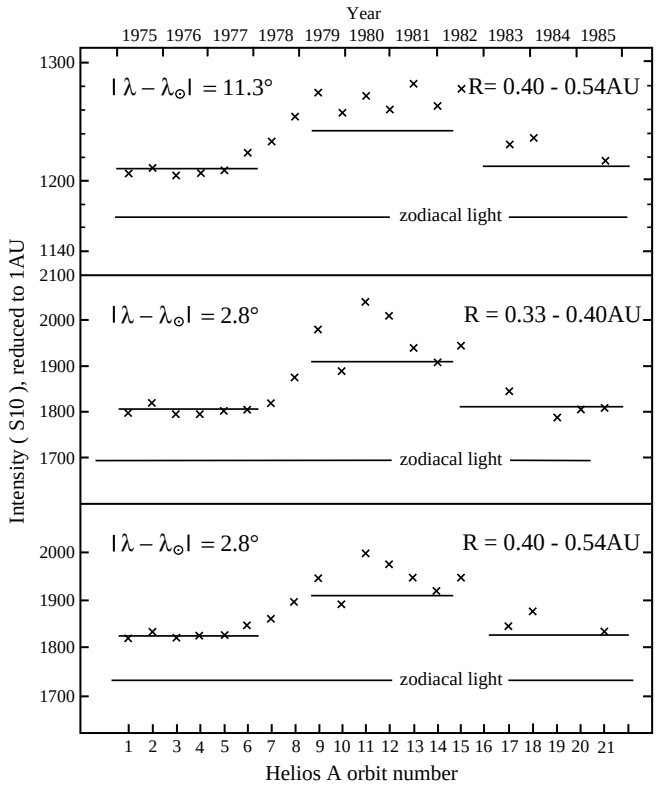

FIG. 5.—Comparison of observed brightness increase during solar maximum with model predictions ($X = 2$, $Y = -2.1$; see text). The data are shown as crosses, the model predictions as horizontal lines, where the baseline following from the model also is included, labeled as "zodiacal light." The two lower panels show the viewing direction over the south pole of the Sun (sectors 1 and 32), and the top panel shows the next viewing directions following to the east and west (sectors 3 and 4, 30 and 31). The heliocentric distance range along the *Helios* orbit over which the photometric data have been averaged is also indicated.

that move approximately radially outward from the Sun. The filtered data show these events and can be used to form images of transient phenomena in the heliosphere. Such images have been used to trace the extent of coronal mass ejections and other lower corona phenomena normally viewed by coronagraph techniques (Jackson 1985; Jackson & Leinert 1985; Jackson 1986; Webb & Jackson 1990; Jackson 1991). By displaying the *Helios* photometer data with time, as measured at a given longitude in the *Helios* orbit and at the same specific viewing direction, a truly differential comparison from orbit to orbit is possible, and any long-term changes in the data can be noted. Figure 4 (reproduced from Leinert & Pitz 1989) is a specific example of this type of data display.

Figure 4 clearly shows an increase in brightness for the sectors that look above the solar poles nearest the solar longitude during the time of solar maximum around 1980, followed by a return to original brightness levels afterward. The difference in these observations from those of the lower corona (which show a similar brightness enhancement over the solar poles at solar maximum) is that the *Helios* photometers measure line-of-sight density variations at heliocentric distances greater than 18 $R_\odot$, above the region of primary solar wind acceleration. These measurements are obtained at approximately the same height above the Sun as the IPS measurements of solar wind speed described in § 2.2. We assume that this long-term brightness change is due solely to Thomson scattering from electrons, a conclusion also justified by the lack of variation at 63° elongation from the Sun (Fig. 4), where the interplanetary plasma contribution to the observed zodiacal light signal is much smaller. Measurements of bright star crossings through the *Helios* fields of view throughout the lifetime of the photometers allow an absolute calibration to within 4%–5% (Leinert et al. 1981b). The actual long-term stability of the photometers is thought to be far better than this ($\leq 1\%$). As depicted in Figure 4, we note the stability of the photometer that over 12 yr gave the same readings for the bright star α CMi to within $\approx 1\%$.

Figure 5 presents examples of the data used for the present study. In order to measure changes in the electron number unbiased by the factor of 10 change in zodiacal light brightness along each *Helios* orbit, we average data from the same orbital positions and fields of view every orbit. All the data display the signal to be explained here, a substantial brightness increase during solar maximum. In order to compare the data shown in one part of the orbit to those from another part (Fig. 5), all measurements have been reduced to 1 AU by correcting them for the radial brightness dependence proportional to $r^{-2.3}$ found for the zodiacal light. The S10 unit used here is equivalent to one solar-type star of 10 mag per square degree, and for measurements with the *Helios* blue filter ($\lambda_{\rm eff} = 428$ nm) corresponds to 1.029×10^{-8} W m^{-2} sr^{-1} μm^{-1}. We averaged data from 20° intervals of each *Helios* orbit and indicate these in terms of spacecraft heliocentric distance for the data sets presented in Figure 5. In addition, for $|\lambda - \lambda_\odot| = 2\overset{\circ}{.}8$, the two $5\overset{\circ}{.}6$ sectors nearest the solar poles (1 and 32) were averaged. For $|\lambda - \lambda_\odot| = 11\overset{\circ}{.}3$, the averages include a total of four $5\overset{\circ}{.}6$ sectors (2, 3, 30, and 31) from longitudes on either side of the Sun. These averages (Fig. 5, *crosses*) retain considerable scatter because of the ever-changing activity of solar wind, but there is no doubt about the brightness increase during solar maximum. To determine solar cycle

TABLE 1

EXCESS ELECTRON SCATTERED LIGHT AT SOLAR MAXIMUM[a]

ELONGATION OF FOV (deg) (1)	*Helios* 1, $\beta = -16\overset{\circ}{.}2$				*Helios* 2, $\beta = +16\overset{\circ}{.}2$			
	Observed[b] (2)	Predicted[d] (3)	Ratio (4)	CMEs (%) (5)	Observed[c] (6)	Predicted[d] (7)	Ratio (8)	CMEs (%) (9)
16.4	132	102	1.29	14	140	70	2.00	51
19.6	55	39	1.41	18	62	39	1.60	27

[a] In S10 units, reduced to 1 AU, averaged over the inner part of the *Helios* orbits, $R \leq 0.5$ AU.
[b] Observations through polarized foil, oriented at position angle −92°.
[c] Observations of total brightness.
[d] Predicted for an $X = 2.0$, $Y = -2.1$ model.

changes, we grouped the data by minimum and maximum years. Orbits 1–6 were averaged to represent minimum conditions, while orbits 9–14 were averaged to represent solar maximum.

While a breakdown into smaller temporal and spatial intervals would be possible, we decided to average the data in this way because it allows a simple comparison with global solar cycle changes. These averaged *Helios* brightness differences are shown in Table 1, and are used for comparison with the models determined from the data of the two previous sections, as described below.

3. THE SOLAR WIND MODEL

We interpret the observed solar cycle changes in brightness in terms of a global solar wind model in which the radial and latitudinal dependences are factored as

$$n_e(r, \theta) = n_0 r^Y f(\theta) , \quad (1)$$

where $n_e(r, \theta)$ is the electron density at heliocentric distance r and heliographic latitude θ, n_0 is the electron density at 1 AU in the ecliptic, r is in AU, and $f(\theta)$ gives the latitudinal decrease of electron density. Varying the power Y allows us to explore density falloffs with heliospheric distance different from a pure inverse square expansion ($Y = -2$). That this falloff is given approximately by a power-law radial dependence is shown by *Helios* in situ measurements (see Bougeret, King, & Schwenn 1984). Schwenn (1990) also gives information that can be used to determine the parameter Y if we assume that each proton is associated with an average of 1.06 electrons and that the changes from this value (derived from the α/n_p ratio) are not significant for our study. In this case, an average value of $Y = -2.1$ results. A value of $Y = -2.1$ requires an acceleration of the solar wind between 0.1 AU (the closest approach of the *Helios* photometer field of view to the Sun) and 1 AU of $\approx 25\%$.

The latitudinal dependence of electron density was determined from the condition that at any heliocentric distance r,

$$n(r, \theta) V(\theta)^X = \text{constant} . \quad (2)$$

This functional form is motivated by the result mentioned above, that in spatially neighboring solar wind structures, momentum flux, $n_e V^2$, appears to be invariant. For $V(\theta)$, we took the latitudinal velocity dependence derived from the IPS measurement. Taking $X = 2$ (momentum conservation) for our model yields polar electron densities at 1 AU of 3–4 cm^{-3} during minimum, similar to extrapolated values derived from *Ulysses* measurements. Using $X = 3$ (energy flux conservation) predicts somewhat low proton density values of 2–3 cm^{-3}. We also considered other values of X from 0 (isotropy) to 4. These model densities were then used to determine the changes expected in the *Helios* photometer data by integrating the Thomson-scattered brightness (e.g., Billings 1966, p. 150) of all electrons along the line of sight for both minimum and maximum conditions. Since definite solar cycle effects are observed in both the *Helios* and the IPS remotely sensed data, we hoped to match solar cycle brightness changes with reasonable values of X and Y, with $X = 2$, $Y = -2.1$ being the a priori best guess and preferred model. For the photometer data, as mentioned above, we used the average over the years 1975–1977 as typical for solar minimum conditions and approximated conditions during solar maximum by an average over the years 1979–1981.

Because *Helios 1* observations from the 16° photometer are the most extensive, fully covering solar cycle 21, these observations are our primary source of data. Since the *Helios 1* 16° photometer filter wheel became stuck in blue light (on 1979 April 10), and the polarizer became stuck in the position parallel to the ecliptic (on 1978 June 17), for consistency we analyzed the continuing blue polarized light data set for the whole duration of the study. The most pronounced effect of excess brightness during solar maximum is found in those photometer sectors that are directed over the solar poles and at the times when the spacecraft is closest to the Sun. Neither the 31° photometer (which ceased to function after 1979 April 10) nor the 90° photometer on *Helios 1* (which was pointed toward the Large Magellanic Cloud) were as useful for this long-term study.

When modeling the brightnesses of electron scattered light, we took care to repeat the steps involved in the observational data reduction, i.e., the same fields of view, same filter and polarizing foil, same normalization to 1 AU, and we averaged over the same ranges of celestial coordinate locations and *Helios* positions along its orbit. Calculated and observed brightnesses then are on the same scale, quasi-normalized to the observed zodiacal light brightness, and observed and predicted brightness increases during solar maximum can be directly compared.

4. DISCUSSION

We consider two methods for comparing the model predictions to the data: (1) fitting the observations by a suitable choice of model parameters, or (2) using the best-justified model parameters and attempting to find a physical explanation for the remaining difference. Since the model parameters fitting the photometer data have been accurately determined from other measurements (although not globally), we prefer method (2).

Nevertheless, the results of our model fits to the observations using method (1) are instructive. Best fits to the observed difference from solar minimum to solar maximum in the *Helios 1* 16° photometer occurred with model values of $X = 1$, 2, and 3, yielding respective values of $Y = -2.44$, -2.24, and -2.16. No possible solution for X exists with $Y = -2.0$. None of the above fits to the data are satisfactory, since the radial density gradients required to fit the photometer observations are steeper than measured in the solar wind. Alternatively, we take the gradient resulting from the in situ data and determine the best-fitting latitudinal velocity increase. With the value $Y = -2.1$ (from Schwenn 1990), the *Helios 1* 16° photometer data require the parameter $X = 4$, implying a much lower velocity over the solar poles than observed if momentum flux is constant ($X = 2$). In summary, the more reasonable combinations of model parameters do not provide an explanation for the observations over solar cycle 21. Figure 5 shows comparisons using method (2) of the predictions of our best model ($X = 2$, $Y = -2.1$) with the observed brightness changes over solar cycle 21. The use of $X = 2$ in method (2) implies an assumption of momentum flux invariance globally over the solar cycle. We believe that there is ample evidence for this over short periods of time and from one heliospheric structure to the next from other (primarily ecliptic) observations, as cited in the Introduction. In the Figure 5 comparisons, the average modeled brightnesses are fit to the data for the solar minimum, shown as horizontal straight

lines for these years. The predictions made using this model for solar maximum years are similarly shown as horizontal straight lines. The base brightness from solar wind electrons derived by the model is also marked (as "zodiacal light") in Figure 5.

The discrepancy between the photometric data and the predictions of our preferred model with invariant momentum flux indicates an observed brightness greater than expected over the solar pole at solar maximum. We believe that this excess has a different, identifiable physical reason. The *Helios* photometer data were not edited to eliminate any of the brightness known to be caused by discrete ejections of mass (CMEs) present in the solar wind. From earlier work, we expect the total solar wind flux to have about 16% CME mass at solar maximum (Jackson & Howard 1993; Webb & Howard 1994). Since the unexplained excess constitutes a similar percentage of the total predicted model brightness (see Table 1), we presume that this excess is primarily due to the mass of CME-ejected plasma, which is preferentially present at the time of solar maximum. The excess brightness is not a very large percentage of the total, but it is present in all of the *Helios 1* 16° photometer data. Table 1 summarizes the observed and predicted brightness increases from minimum to maximum.

To check these conclusions drawn from the *Helios 1* observations, we also reduced the observations from *Helios 2* from 1976 through 1979. Because the spacecraft was launched at the middle of solar minimum, we do not have as long a baseline at solar minimum in these data. The spacecraft also ceased operating at the middle of solar maximum. The reliability of the results is therefore slightly inferior to those of *Helios 1*. However, when the *Helios 2* in situ densities and IPS velocities are combined in our preferred ($X = 2$, $Y = -2.1$) model and compared with observed brightnesses, we find an even stronger excess at solar maximum over the brightness accounted for by the model. As Table 1 shows, on average this excess amounts to about 50% of the total solar wind brightness for the *Helios 2* photometer data closest to the Sun. This higher value is caused by an anomalously bright seventh orbit of the spacecraft when it was less than 0.5 AU from the Sun during the interval from 1979 April 17 to May 27. A detailed look at the 16° photometer data from *Helios 2* during this interval shows that the data are not smoothly varying, consisting of many bumps of a few days in duration. Jackson et al. (1994) image and list more than 11 CMEs in the data from *Helios 2* during this interval, a far greater number than usual. Two of the CMEs (one beginning at the solar surface on 1979 May 7, another beginning 1979 May 24) are among the most massive CMEs ever observed (Jackson & Webb 1994; Webb et al. 1996). Thus, we have reason to believe that this orbit has an anomalously high brightness contribution from CME mass. This further substantiates the idea that CMEs are the cause of the brightness excess seen with *Helios 1*. The comparison between global solar wind model and brightness observations thus lead us to a twofold result: (1) the assumed invariance of momentum flux provides a reasonable approximation of the global high-latitude solar wind over the solar activity cycle, (2) as long as there is additional mass input during the time of solar maximum, probably through coronal mass ejections.

From our preferred model, we now derive average values of total mass, momentum, and energy fluxes in the solar wind over cycle 21, again assuming a 3.2% solar wind helium abundance (Schwenn 1990). If we denote the average momentum flux m^{-2} as measured in situ by *Helios* as C_0 (to remind us that this is a constant, invariant with heliographic latitude θ), these fluxes can be approximately expressed as

$$\text{mass flux} = \int n_e(\theta) V(\theta) d\Omega \approx \int C_0 / V(\theta) d\Omega \,, \tag{3}$$

$$\text{momentum flux} = \int C_0 \, d\Omega = 4\pi (1 \text{ AU})^2 C_0 \,, \tag{4}$$

$$\text{energy flux} = \int n_e(\theta) V(\theta)^3 \, d\Omega \approx \int C_0 \, V(\theta) d\Omega \,. \tag{5}$$

Results of these integrations are given in Table 2 for solar maximum and solar minimum, and also integrated over the whole cycle. Mass fluxes are highest at maximum, when the velocity is lowest, and the reverse is true for kinetic energy flux. So far, these numbers only refer to the preferred solar wind model. The excess brightness measured in the *Helios* photometer data is the result of additional plasma mass. If these electrons are distributed along the line of sight in approximately the same way as the solar wind density at solar maximum (not an unreasonable assumption for CME mass; see Howard et al. 1985 or Hundhausen, Burkepile, & St. Cyr 1994), then the observed brightness excess is just equal to the percentage of additional plasma mass. (These percentages have been included in cols. [5] and [9] of Table 1 as CMEs.) When we add the same percentages to the integrated fluxes calculated in equations (3)–(5), we obtain

TABLE 2

GLOBAL SOLAR WIND INTEGRALS

Time Interval	Mass Flux		Momentum Flux	Kinetic Energy Flux		Total Energy Flux	
	g s^{-1}	$M_\odot$ yr^{-1}	dyne	ergs s^{-1}	$L_\odot$	ergs s^{-1}	$L_\odot$
At Solar Minimum.....	1.2×10^{12}	1.9×10^{-14}	6.8×10^{19}	2.0×10^{27}	5.3×10^{-7}	4.3×10^{27}	1.1×10^{-6}
At Solar Maximum (without CMEs)	1.4×10^{12}	2.2×10^{-14}	6.2×10^{19}	1.5×10^{27}	3.9×10^{-7}	4.1×10^{27}	1.1×10^{-6}
At Solar Maximum (+20% CMEs)	1.7×10^{12}	2.6×10^{-14}	7.5×10^{19}	1.8×10^{27}	4.6×10^{-7}	4.6×10^{27}	1.2×10^{-6}
	g	$M_\odot$	dyne s	ergs	$M_\odot c^2$	ergs	$M_\odot c^2$
Over Solar Cycle (without CMEs)	4.5×10^{20}	2.2×10^{-13}	2.3×10^{28}	6.4×10^{35}	3.6×10^{-19}	1.5×10^{36}	8.4×10^{-19}
Over Solar Cycle (+20% CMEs)	4.8×10^{20}	2.4×10^{-13}	2.4×10^{28}	6.8×10^{35}	3.8×10^{-19}	1.6×10^{36}	9.0×10^{-19}

an estimate of the actual values of these fluxes during solar cycle 21. These values are also given in Table 2 (last line in each section of the table). In a recent review on global solar magnetic field changes, Wang (1998) used the correlation between coronal holes and high-speed solar wind to predict from solar magnetograms the global pattern of solar wind speed, and hence the variations of total solar wind mass flux over the solar cycle, with similar results.

5. CONCLUSION AND OUTLOOK

We find by combining our three independent types of observations that the concept of constant momentum flux in the heliosphere from solar minimum to solar maximum is a good first approximation. This concept implies that the solar wind is energized equally, not only from one structure to the next but also over the solar cycle. It further implies that the solar wind energization is not greatly affected by the strong solar surface magnetic fields that are predominant at solar maximum. Under the assumption that momentum flux is constant, the mass expelled from the Sun during solar cycle 21 changes from a minimum value of 1.21×10^{12} g s^{-1} to a maximum value of 1.65×10^{12} g s^{-1} globally at solar maximum. This amounts to an expulsion of from 32% to 38% of the total mass of the Sun over time relative to that removed from it in the form of energy by the conversion of mass to energy. At the next level of detail, an excess of the total solar wind density at solar maximum over that of constant momentum flux is seen in the *Helios* photometer data. From observations made using coronagraphs, which allow an estimate of total CME masses from individual events, we expect perhaps as much as 16% of the total solar wind mass to be present at solar maximum in the form of CME mass. With the assumption that solar wind momentum flux is constant, and that the excess density on average is distributed in solar longitude in the same manner as the solar wind electrons, the brightness excess observed by the *Helios* photometers also gives an estimate of the total excess mass expelled into the solar wind. We find that this solar wind excess or CME mass amounts to $\approx$18% of the total solar wind mass at solar maximum for *Helios 1* during cycle 21; an even larger percentage is derived from *Helios 2* measurements. The quantity of the excess mass, derived here in a fundamentally different approach, is thus approximately the same as that for CMEs measured by coronagraphs. The quantitatively very close agreement of the two results, however, appears to be fortuitous. Both quantities estimated by our analysis are basic to the solar wind. We have no reason to believe that the total amount of solar wind momentum flux over solar cycle 21 is different during the present solar cycle. However, the solar wind mass present in the form of CME material, which changes with solar activity, may differ from one solar cycle to the next. The measurements presented here give an estimate of the percentage of this total CME mass during solar cycle 21. The separation of these two phenomena makes us think that they are caused by two different processes, and that there are at least two mechanisms at work in releasing solar wind mass globally around the Sun.

Ch. Leinert, principal investigator on the *Helios* zodiacal light experiment, would like to acknowledge support for the reduction of the zodiacal light photometer data from the Bundesministerium für Forschung und Technologie, grant WRS 0108, and Susanne Lindauer for help with the analysis presented in this paper. The work of B. Jackson was partially supported by grant AFOSR-94-0070 to the University of California at San Diego. B. Jackson would like to express his appreciation to his colleagues and the staff of the Max-Planck-Institute für Astronomie for supporting this work and for partial salary during his recent stay as a visiting research scholar. Both of us thank Rainer Schwenn for helpful comments and discussions.

REFERENCES

Bame, S. J., Asbridge, J. R., Feldman, W. C., & Gosling, J. T. 1976, ApJ, 207, 977
Bertaux, J. L., & Lallement, R. 1984, A&A, 140, 230
Billings, D. E. 1966, A Guide to the Solar Corona (New York: Academic)
Bougeret, J. L., King, J. H., & Schwenn, R. 1984, Sol. Phys., 90, 401
Bruno, R., Villante, U., Bravassano, B., Schwenn, R., & Mariani, F. 1986, Sol. Phys., 104, 431
Coles, W. A., & Kaufman, J. J. 1978, Radio Sci., 13, 591
Coles, W. A., et al. 1980, Nature, 286, 239
de Jager, C., Nieuwenhuijzen, H., & van der Hucht, K. A. 1984, in Instabilities in Luminous Early Type Stars, ed. H. J. G. L. M. Lamers & C. W. H. de Loore (Dordrecht: Reidel), 201
Goldstein, B. E., et al. 1996, A&A, 316, 296
Hewish, A., Scott, P. F., & Wills, D. 1964, Nature, 203, 1214
Hick, P. L., & Jackson, B. V. 1994, Adv. Space Res., 14(4), 135
Hick, P. L., Jackson, B. V., Rappoport, S., Woan, G., Slater, G., Strong, K., & Uchida, Y. 1995, Geophys. Res. Lett., 22, 643
Howard, R. A., Sheeley, N. R., Jr., Koomen, M. J., & Michels, D. J. 1985, J. Geophys. Res., 90, 8173
Hundhausen, A. J., Burkepile, J. T., & St. Cyr, O. S. 1994, J. Geophys. Res., 99, 6543
Jackson, B. V. 1985, Sol. Phys., 100, 563
———. 1986, Adv. Space Res., 6, 307
———. 1991, J. Geophys. Res., 96, 11307
Jackson, B. V., Hick, P. L., Kojima, M., & Yokobe, A. 1998, J. Geophys. Res., 103, 12049
Jackson, B. V., Hick, P., Leinert, Ch., & Yokobe, A. 1998, BAAS, 30, 846
Jackson, B. V., & Howard, R. A. 1993, Sol. Phys., 148, 359
Jackson, B. V., & Leinert, C. 1985, J. Geophys. Res., 90, 10759
Jackson, B. V., & Webb, D. F. 1994, in Proc. 3d SOHO Workshop on Solar Dynamic Phenomena & Solar Wind Consequences (ESA SP-373) (Paris: ESA), 233
Jackson, B. V., Webb, D. F., Hick, P. L., & Nelson, J. L. 1994, Hanscom Air Force Base, FBPL–TR–94–2040 (U.S. Air Force)
Kojima, M., Tokumaru, M., Watanabe, H., Yokobe, A., Asai, K., Jackson, B. V., & Hick, P. L. 1998, J. Geophys. Res., 103, 1981
Lallement, R., Bertaux, J. L., & Kurt, V. G. 1985, J. Geophys. Res., 90, 1413
Lallement, R., Bertaux, J. L., Kurt, V. G., & Mironova, E. N. 1984, A&A, 140, 243
Leinert, C., Link, H., Pitz, E., Salm, N., & Klüppelberg, D. 1975, Raumfahrtforschung, 19, 264
Leinert, Ch., & Pitz, E. 1989, A&A, 210, 399
Leinert, C., Pitz, E., Link, H., & Salm, N. 1981a, Space Sci. Instrum., 5, 257
Leinert, Ch., Richter, I., Pitz, E., & Planck, B. 1981b, A&A, 103, 177
Mullan, D. J. 1983, ApJ, 272, 325
Munro, R. H., & Jackson, B. V. 1977, ApJ, 213, 874
Phillips, J. L., et al. 1995, Science, 268, 1030
Richter, I., Leinert, C., & Planck, B. 1982, A&A, 110, 115
Rickett, B. J., & Coles, W. A. 1991, J. Geophys. Res., 96, 1717
Schwenn, R. 1990, in Physics of the Inner Heliosphere 1, ed. R. Schwenn & E. Marsch (Berlin: Springer), 99
Solar Geophysical Data. 1982, Prompt Reports (Pt. 1), 452, 13
———. 1987, Prompt Reports (Pt. 1), 515, 9
Steinitz, R., & Eyni, M. 1980, ApJ, 241, 417
Uchida, Y., McAllister, A., Strong, K. T., Ogawara, Y., Shimizu, T., Matsumoto, R., & Hudson, H. S. 1992, Publ. Astron. Soc. Japan, 44, L155
Wang, Y.-M. 1997, in Proc. 10th Cambridge Workshop on Cool Stars, Stellar Systems and the Sun (Cambridge: Cambridge Univ. Press), in press
Webb, D. F., & Howard, R. A. 1994, J. Geophys. Res., 99, 4201
Webb, D. F., Howard, R. A., & Jackson, B. V. 1996, in AIP Conf. Proc. 382, Solar Wind Eight, ed. D. Winterhalter et al. (Woodbury: AIP), 540
Webb, D. F., & Jackson, B. V. 1990, J. Geophys. Res., 95, 20641
———. 1992, in Solar Wind Seven, ed. E. Marsch & R. Schwenn (Oxford: Pergamon), 623